JACS
JOURNAL OF THE AMERICAN CHEMICAL SOCIETY
Article
pubs.acs.org/JACS

Probing Nucleation Pathways for Morphological Manipulation of Platinum Nanocrystals

Tao Yao,[†,§] Shoujie Liu,[‡,§] Zhihu Sun,[†] Yuanyuan Li,[†] Shi He,[‡] Hao Cheng,[†] Yi Xie,*[,‡] Qinghua Liu,[†] Yong Jiang,[†] Ziyu Wu,*[,†] Zhiyun Pan,[†] Wensheng Yan,[†] and Shiqiang Wei*[,†]

[†]National Synchrotron Radiation Laboratory, University of Science and Technology of China, Hefei 230029, China

[‡]Department of Nanomaterials and Nanochemistry, Hefei National Laboratory for Physical Sciences at Microscale, University of Science and Technology of China, Hefei 230026, China

Supporting Information

ABSTRACT: Understanding the formation process in the controlled synthesis of nanocrystals will lead to the effective manipulation of the morphologies and properties of nanomaterials. Here, *in-situ* UV−vis and X-ray absorption spectroscopies are combined to monitor the tracks of the nucleation pathways in the solution synthesis of platinum nanocrystals. We find experimentally that the control over nucleation pathways through changing the strength of reductants can be efficiently used to manipulate the resultant nanocrystal shapes. The *in-situ* measurements show that two different nucleation events involving the formation of one-dimensional "Pt_nCl_x" complexes from the polymerization of linear "$Cl_3Pt-PtCl_3$" dimers and spherical "Pt_n^0" clusters from the aggregation of Pt^0 atoms occur for the cases of weak and strong reductants; and the resultant morphologies are nanowires and nanospheres, respectively. This study provides a crucial insight into the correlation between the particle shapes and nucleation pathways of nanomaterials.

INTRODUCTION

The controlled synthesis of Pt nanocrystals (NCs) has provided an attractive routine in tailoring the catalytic activity and selectivity of the Pt nanostructures in widespread practice applications, e.g., fuel cell, hydrogen production, and gas sensing.[1−5] Among many synthesis strategies, the chemical reduction method involving a metallic precursor and a reductant has become a preferred one for preparing NCs with well-defined shapes.[6−8] Through fine-tuning the reagents and reaction conditions, nanostructures with a wide variety of morphologies ranging from 0-dimensional (0D) nanospheres to 1D nanowires have been achieved,[6,9−14] as illustrated in Figure 1a. Despite the remarkable advances in the synthesis of colloidal NCs, our abilities of manipulation on their formation processes, particularly the state of nascent nuclei in the nucleation process and chemical reduction, stay on the empirical level and remain a great challenge.[9,11,15,16]

The initial nucleation is a central step to the following growth process and the resultant morphology of the NCs under the given conditions, but it is rather difficult to structurally determine and further control over the newly formed tiny clusters. Therefore, the study on the nucleation kinetics has long been a hot topic since the classical nucleation theory proposed by LaMer.[17] Recently, some experimental and theoretical reports have given some hints for the existence of dimeric complexes toward higher nuclearity metal species.[18−20] Furthermore, the reliable kinetic evidence for the dimeric species has been demonstrated by fitting the kinetic data quantitatively on the basis of an autocatalytic reduction−nucleation.[21,22] However, the experimental "*in-situ*" tools capable of capturing and identifying the nuclei are more requisite to support these kinetically competent intermediates.

In addition, the reductant may provide possible access to control nucleation kinetics, since the reductant serves the role of reducing metallic precursors into monomeric units, which is the first step in the nucleation.[10,23,24] For instance, it is reported that, through a proper choice of reductants with different reducing capacities, the reduction process can be manipulated to synthesize various NC's morphologies.[10] Unfortunately, the mechanism of reductant-led nucleation responsible for the formation of a specific shape remains unclear, or it is based on the qualitative hypothesis or the theoretical calculations. Recently, the *in-situ* TEM has been used to observe the grain growth of Pt NCs with the size of about 2 nm.[25] Nevertheless, it is still difficult to uncover the initial nucleation in the formation of NCs. More recently, the initial nucleation mechanism of Au clusters with size less than 1 nm has been uncovered by *in-situ* X-ray absorption fine structure (XAFS), showing the reduction process via the formation of an intermediate $Cl_3^-Au-AuCl_3^-$ dimer in the reaction solution.[26] Time-dependent XAFS measurement performed in an *in-situ* manner is one of the most powerful tools to study the dynamic structural changes of materials, and it has been widely applied to monitor the formation process of metal particles.[27−29]

Received: March 19, 2012
Published: May 14, 2012

   dx.doi.org/10.1021/ja302642x | *J. Am. Chem. Soc.* 2012, 134, 9410−9416

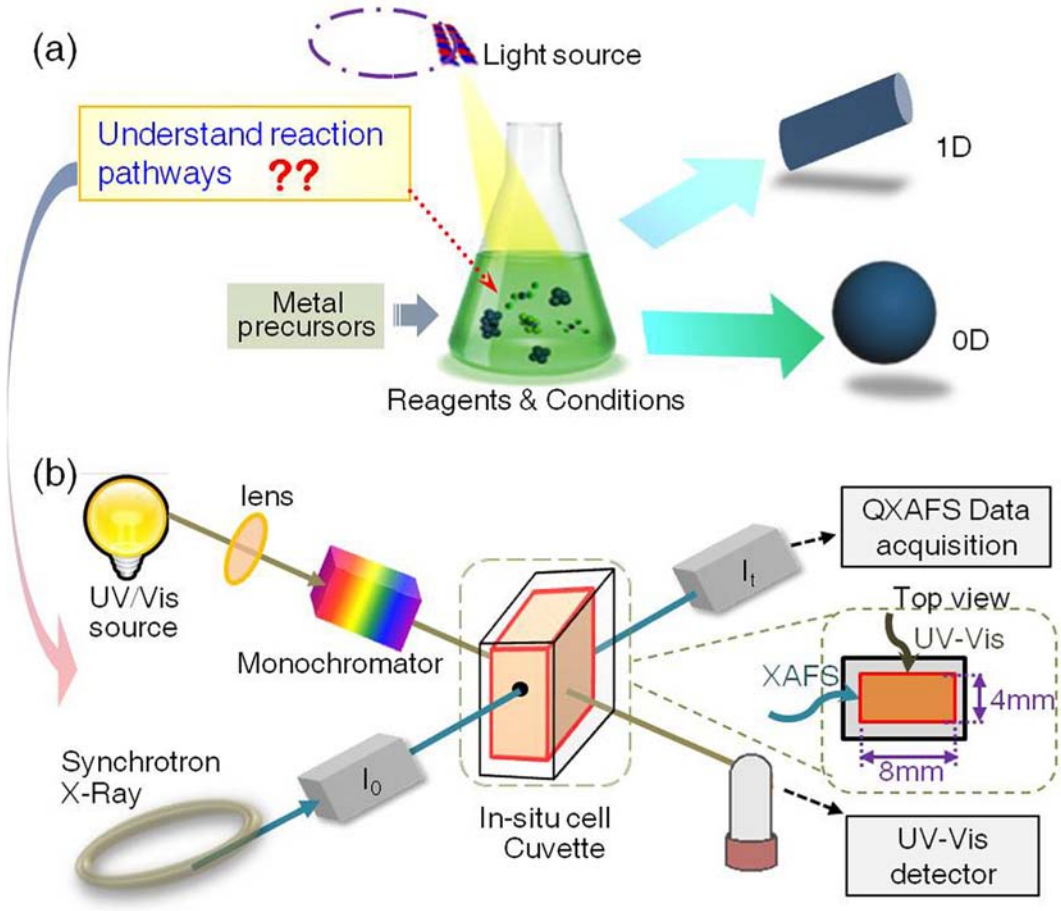

Figure 1. (a) Schematic showing the pressing requirement of understanding kinetic reation pathways for the controlled synthesis of nanostructures with various mophologies, such as 0D and 1D nanostructures. (b) Experimental setup of the multi-*in-situ* techniques combining UV−vis and quick-XAFS. The reaction solution was continuously circulated along the tubes into and out of the quartz cuvette by peristaltic pump to achieve the *in-situ* measurements. The UV−vis and XAFS data are measured simultaneously for ∼70 s.

In this work, we take the advantage of *in-situ* measurements combining quick-XAFS and UV−vis spectroscopies to probe the nucleation pathways of solution-synthesized Pt NCs. The combined probing system could offer a comprehensive study on nucleation and growth of nanoparticles.[30,31] Compared with our previous work, we here not only reveal the details on the nucleation pathways but also experimentally elucidate the mechanism by which the nucleation pathways can be mediated to influence the resultant shapes. Shown in Figure 1b is the schematic layout of an experimental setup, which permits the simultaneous determination of the structural information and species evolution by a combination of *in-situ* XAFS and UV−vis absorption spectroscopies. The *in-situ* studies show that nucleation pathways of Pt NCs are strongly correlated with the strength of the used reductants. As a result, the obtained Pt NCs possess different shapes which show the thermodynamically favored sphere and kinetically controlled wirelike morphologies. These measurements highlight an important role of reductant in mediating the nucleation processes and pave a new way for the controllable synthesis of nanostructures.

■ EXPERIMENTAL SECTION

Chemicals. Potassium tetrachloroplatinate(II) (K_2PtCl_4, 99.9% trace metals basis, Aldrich) was used as precursor. Citric acid (Aldrich) and ethylene glycol (Aldrich) were used as reducing agents. Poly(vinylpyrrolidone) (PVP, MW = 55000, Aldrich) was used as stabilizer for both reactions.

Synthesis of Platinum Nanocrystals. *Synthesis of Pt NCs Reduced by Ethylene Glycol.* In a typical synthesis, 0.16 mmol of K_2PtCl_4 and 0.09 g of PVP were separately dissolved in 4 mL of ethylene glycol at room temperature. These two solutions were then added simultaneously to the three-neck flask (equipped with a reflux condenser and a magnetic stirring bar) containing 8 mL of ethylene glycol. The mixture was then heated to 60 °C in air. The concentration of K_2PtCl_4 was fixed at 10 mM. The product was collected by centrifugation and washed with ethanol several times to remove ethylene glycol and excess PVP.

Synthesis of Pt NCs Reduced by Citric Acid. Here, the reducing agent was replaced with citric acid. Briefly, the mixture solution containing 0.16 mmol of K_2PtCl_4, 0.09 g of PVP, and 153 mg of citric acid was placed in a three-neck flask. Here, water was used as solvent in this reaction for dissolving reductant CA powder and other reagents, which would have little influence on the reaction and the *in-situ* UV−vis results. The solution was also heated to 60 °C in air.

***In-Situ* Measurement.** The UV−vis and quick-XAFS data were collected at U7C station in NSRL (National Synchrotron Radiation Laboratory, P.R. China) and 1W1B station in BSRF (Beijing Synchrotron Radiation Facility, P.R. China). The storage rings of NSRL and BSRF were operated at 0.8 GeV with the maximum current of 200 mA and at 2.5 GeV with the maximum current of 450 mA, respectively. *In-situ* quick XAFS measurements at the Pt L_3-edge were performed in transmission mode, using ionization chambers with optimized detecting gases to measure the radiation intensity (incident intensity I_0 and transmitted intensity I_t). The XAFS data were

dx.doi.org/10.1021/ja302642x | J. Am. Chem. Soc. 2012, 134, 9410−9416

collected up to about 1000 eV past the absorption edge. An approximate X-ray photon flux of 10^{11} photons/s was monochromatized using a Si(111) monochromator which was moved quickly to achieve the quick measurement (about 70 s for a spectral scan). The UV−vis spectra (in the range 200−600 nm) were collected in transmission, perpendicular to the incident X-ray beam, using a TU-9001 spectrometer equipped with a lens and a monochromator. This spectrometer is able to collect a complete UV−vis absorption spectrum in 70 s, almost comparable with that for quick-XAFS.

***In-Situ* Cell.** The reactive solution prepared by the procedure mentioned above was continuously circulated along the microtubes by peristaltic pump and flowed into a specially designed quartz cuvette during the acquisition of UV−vis and XAFS spectra. To reach the optimum absorption thickness and obtain good signal-to-noise data for XAFS measurement, the cuvette has a path length in the X-ray direction of 8 mm, while the path length in the UV−vis direction is designed as 4 mm. The thickness of the transparent quartz windows in the X-ray direction is 100 μm to minimize the X-ray absorption of the windows at the energy of the Pt L_3-edge. The UV−vis data were collected continuously parallel to the XAFS measurements.

XAFS Data Analysis. The acquired EXAFS data were processed according to the standard procedures using the ATHENA module implemented in the IFEFFIT software packages.[32] The k^2-weighted EXAFS spectra were obtained by subtracting the postedge background from the overall absorption and then normalizing with respect to the edge−jump step. Subsequently, k^2-weighted $\chi(k)$ data in the k-space ranging from 2.2 to 12.7 Å^{-1} were Fourier transformed to real (R) space using hanning windows (dk = 1.0 Å^{-1}) to separate the EXAFS contributions from different coordination shells. The R_{bkg} value of 1.0 was used for all samples. The quantitative analysis was carried out using the ARTEMIS module.[33] The backscattering amplitude $F_i(k_i)$ and phase shift $\Phi_i(k_i)$ were calculated using FEFF8.4 code. Multiple scattering was included up to the third order. During the curve-fitting, the overall amplitude reduction factor S_0^2 was fixed to be the best-fit value of 0.86, determined from fitting the reference metal Pt foils. The nearest Pt−Cl and Pt−Pt shells in the R-range of 1.5−3.3 Å and the k-range of 2.2−12.7 Å^{-1} were included in the fitting. The Pt−Pt scatting path with the coordination number and bond distance of N = 12 and R = 2.77 Å in the fcc−structured Pt bulk were used in the fit of the Pt−Pt shell. The Pt−Cl scatting path with the coordination number and bond distance of N = 4 and R = 2.33 Å in a K_2PtCl_4 structure were used in the fit of the Pt−Cl shell. The structural parameters, such as the coordination number N, the interatomic distance R, the Debye−Waller factor σ^2, and the edge−energy shift ΔE_0, were allowed to vary during the fitting process.

RESULTS AND DISCUSSION

For the reduction method synthesizing noble metal NCs, the initial nucleation involving the reduction of precursor compounds and the subsequent aggregation can be summarized as two different pathways.[11,15] One is the partial reduction of precursor ions first to some intermediate complex without experiencing the zerovalent state; the other is the complete reduction of precursor ions into zerovalent atoms followed by their aggregation to nuclei. These two pathways are schematically shown as equations in Figure S1 (Supporting Information). Depending on the strength of the reductants, the reduction rate may be tuned in a controllable manner. To achieve the switch of initial nucleation between two pathways, we selected ethylene glycol (EG) and citric acid (CA) as representatives of a weak and a strong reductant to reduce the $PtCl_4^{2-}$ ions (two reactions are denoted as EG reduction and CA reduction hereafter, respectively). As a consequence, the obtained NCs possess different morphologies, i.e. a wirelike and a spherical shape (Figure 2a and b) for the EG and CA reduction, respectively.

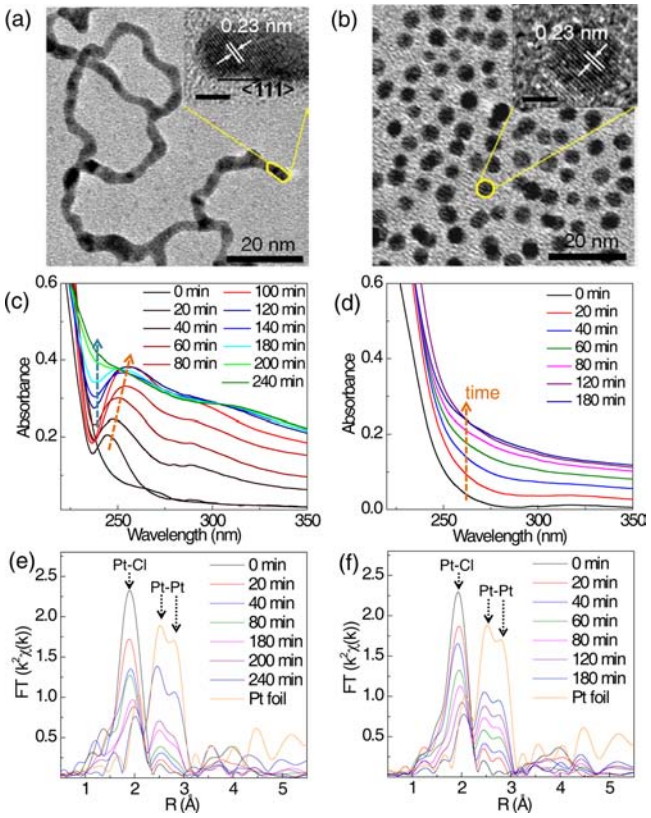

Figure 2. Two representative mophologies, i.e., nanowires (a) and nanospheres (b) synthesized by using ethylene glycol and citric acid, respectively. Their HRTEM images are shown in the inset (scale bar = 2 nm). Temporal evolution of UV−vis absorption spectra of Pt colliod solutions for the K_2PtCl_4 reduced by ethylene glycol (c) and citric acid (d). Time variations in k^2-weighted EXAFS Fourier transform spectra during the reaction processes of the K_2PtCl_4 reduced by ethylene glycol (e) and citric acid (f).

To reveal the mechanism of how the reductant-controlled nucleation influences the final morphology, we performed *in-situ* measurements of the reduction kinetics for two reaction processes. The *in-situ* UV−vis absorption spectra monitoring the formation processes of Pt NCs are shown in Figure 2c and d. For both initial mixture solutions, the UV−vis spectra display the same featureless curves in the wavelength range of 220−350 nm. The precursor $PtCl_4^{2-}$ ions only show the maximum at around 220 nm (Figure S2, Supporting Information), due to the metal-to-ligand (Pt−Cl) charger transfer.[34,35] At the end of both reactions, the broad and featureless absorption in the spectra with higher absorption baseline in the low wavelength region can be attested to the interband transition of the formed colloidal Pt particles (Supporting Information Figure S2).[36] However, the time-dependent evolutions of the spectral features in the 245 to 255 nm range are remarkably different for the two reactions, pointing out the occurrence of different reduction routes. For the case of EG as the reducing agent, a peak at 245 nm appears at the early stage, increasing and shifting to higher wavelengths (255 nm) vs time in the first 100 min (Figure 2c). As the reaction proceeds, the intensity of this intermediate absorbance gradually decreases and finally disappears. On the contrary, when CA is used as the reductant, the UV−vis spectra shown in Figure 2d display a monotonic transition from the initial precursor to final NCs with the reaction time, without the appearance of any additional peaks.

dx.doi.org/10.1021/ja302642x | J. Am. Chem. Soc. 2012, 134, 9410−9416

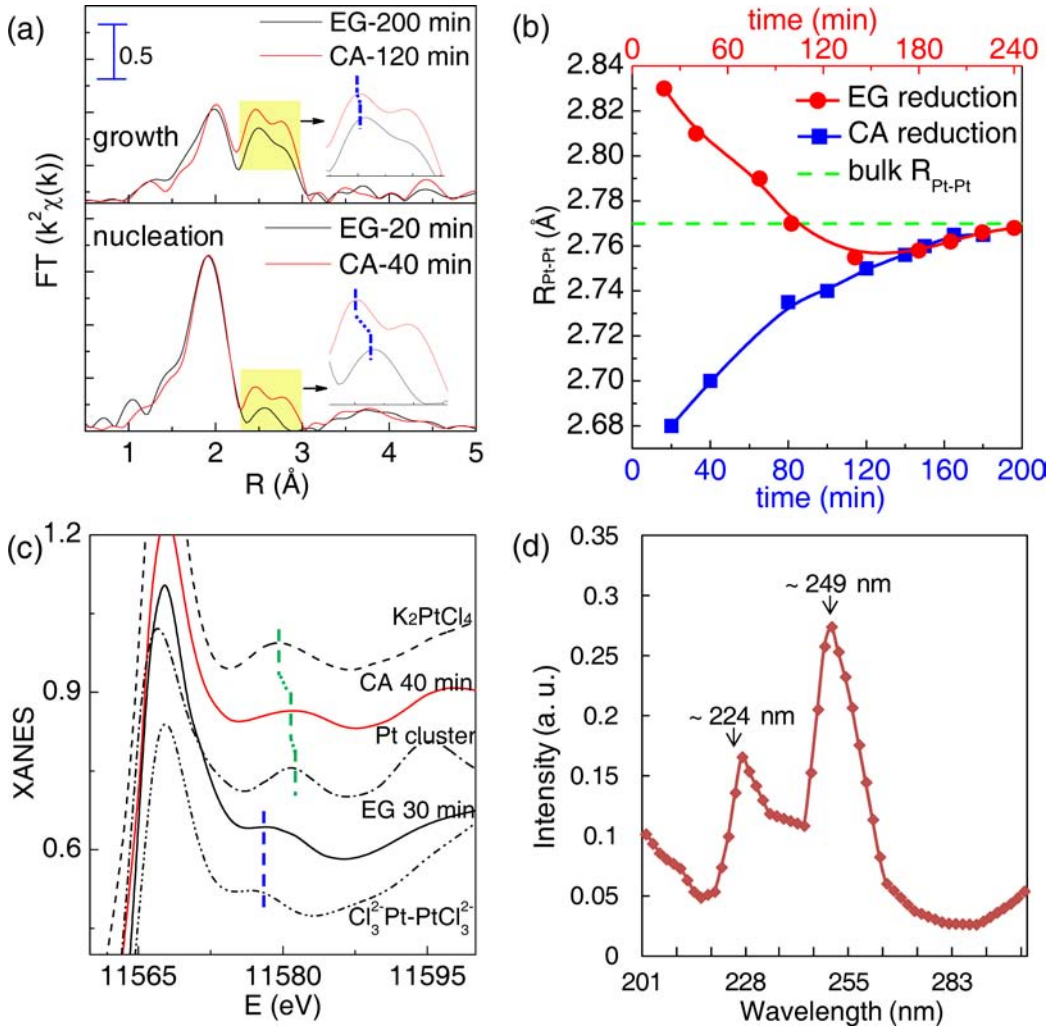

Figure 3. (a) Comparison of the Fourier transform spectra at the representative time points in the nucleation and the growth processes for the two reactions. (b) Time profiles of Pt−Pt bond lengths from the EXAFS fitting for the K_2PtCl_4 reduced by ethylene glycol (red) and citric acid (blue). The bulk Pt−Pt bond length is shown as the reference (dash green). (c) Pt L_3-edge XANES calculations for various Pt clusters and experimental spectra in the initial nucleation. The structural model of the naked Pt_n^0 cluster adopts the most stable configurations. The $Cl_3^{2-}Pt-PtCl_3^{2-}$ dimer is assumed to arise from two partially reduced $PtCl_3^{2-}$ ions connected via a Pt−Pt bond. (d) The density functional theory calculations of the absorption spectrum of the $Cl_3^{2-}Pt-PtCl_3^{2-}$ dimer.

The new features in Figure 2c in the range 245−255 nm cannot be simply assigned to the $PtCl_4^{2-}$ or naked Pt_n^0 clusters because both are featureless in this wavelength region. Instead, they could originate from some Pt-contained complexes. One possible product is the complex of Pt clusters with the ligands, such as the amide of the PVP or EG, in which the Pt−amide charge transfer may lead to the appearance of ∼250 nm absorbance. This is partly similar to the previous observation of a new absorbance peak at ∼250 nm that is attributed to ligand-to-metal charge transfer in the Pt^{2+}/dendrimer complex.[37] Another possibility accounting for the ∼250 nm absorbance is the formation of the "Pt_nCl_x" complex produced from nucleation pathway 1, as we have described above (Supporting Information Figure S1). These distinct Pt clusters bonded with Cl ions may change the electronic structure from their zerovalent clusters, leading to the generation of intermediate absorbance. When CA is used as the reducing agent, no absorbance attributed to any intermediate complexation can be found in Figure 2d. Differences between the UV−vis results of the two reactions imply the strong dependence of nucleation process on the strength of the reductants.

To distinguish the intermediate species and to obtain structural information associated with the reaction processes, we performed *in-situ* Pt L_3-edge XAFS measurements on the reacted solutions. A complete reduction of $PtCl_4^{2-}$ to Pt NCs can be clearly recognized by the progressive variations of oscillation shape and the enhanced amplitude in the k range above 10 $Å^{-1}$, as shown by extended XAFS (EXAFS) data with a high signal-to-noise ratio (Supporting Information Figure S3). The Fourier transforms (FTs) of EXAFS data (see Figure 2e and f) demonstrate a common trend that the intensity of the peak at 1.94 Å ascribed to the first Pt−Cl shell gradually decreases, while the peaks in the range of 2.3−3.0 Å assigned to the first Pt−Pt shell appear and enhance with time. However, after a closer inspection one can find that the position of the Pt−Pt peak (2.56 Å) formed in the early nucleation is longer than that of the Pt foil (2.51 Å) and shifts to the low R side vs time for EG reduction (Figure 2e), while there is a converse evolution for CA reduction (Figure 2f). We also compare the Pt−Pt peak positions in FTs for the representative initial nucleation and later growth stages of both reactions (Figure 3a). The position of the Pt−Pt peak for the EG reduction (2.56

dx.doi.org/10.1021/ja302642x | J. Am. Chem. Soc. 2012, 134, 9410−9416

Å) is higher than that of the main peak (2.45 Å) for the CA reduction. The temporal evolution of the extracted Pt−Pt bond length from quantitative curve-fittings (curves and parameters shown in Figures S4 and S5 and Table S1 of the Supporting Information) as a function of reaction time is displayed in Figure 3b. The most interesting finding is that the Pt−Pt bond length undergoes greatly different trends as the reaction proceeds. Within the first 100 min, the Pt−Pt bond length for EG reduction shows a gradual decrease starting from 2.83 Å toward the Pt bulk value (2.77 Å), while the Pt−Pt bond length for CA reduction exhibits a steady growth from an initial value of 2.68 Å. It appears that, in conjunction with UV−vis absorption spectra, two different intermediate Pt clusters with significantly different Pt−Pt coordination environments are formed in these two reactions.

We would then examine the possible Pt-contained species, particularly for the EG reduction in which the new absorbance at ∼250 nm appears in UV−vis spectra. It should be noted that the Pt−Cl and Pt−O bonds can be clearly distinguished in EXAFS (Supporting Information Figure S6), and the position of the Pt−O peak is 0.4 Å smaller than that of Pt−Cl, since a Cl atom scatters X-ray more strongly than the O atom. It can be found that, for the whole process of two reactions, no obvious contribution from the Pt−O pair can be observed in the FT curves. Hence, it is safe to assert that there are no strong chemical absorptions of surfactant PVP or EG on the Pt-contained complexes, since PVP and the oxidation product of EG are both terminated with the hydroxyl (−OH) group. The weak chemical absorption means long and irregular distances between Pt and O, which leads to the absence of the Pt−O peak in the EXAFS spectra. In addition, the contribution of the hydrolysis product $PtCl_2(H_2O)_2$ from the ligand-exchange between Cl^- and H_2O can also be neglected. Therefore, the first possible mechanism described above that Pt-amide charge transfer leads to the appearance of intermediate ∼250 nm absorbance in UV−vis spectra can be excluded. On the other hand, it is well-known that the small naked metal clusters show an obvious bond length contraction with respect to their bulk counterpart.[38,39] Then, it is reasonable that Pt−Pt bond length shortening in the case of CA reduction is from the initially formed naked Pt_n^0 nuclei with very small sizes, while the different bond lengths for the Pt−Pt pair for the EG reduction cannot be simply assigned to the naked Pt_n^0 clusters. Combining the above analysis, we consider that the ∼250 nm absorbance may be from the "Pt_nCl_x" polymer complexes, and the charge transfer between Pt and surrounding Cl ions may lead to the expansion of Pt−Pt bond length, which is also predicted from the theoretic calculations by Ciacchi et al.[18] Further, the obtained coordination number of the Pt−Pt shell in Supporting Information Table S1 for the EG reduction at 20 min is 1.2, implying the formation of $Cl_3^{2-}Pt-PtCl_3^{2-}$ dimer as the main species at this reaction time.

To further verify this hypothesis, we perform the X-ray absorption near-edge structure (XANES) simulations for the typical dimer cluster $Cl_3^{2-}Pt-PtCl_3^{2-}$ (Figure 3c). Its configuration was optimized following the same procedure reported in our previous work.[26] We found that the spectrum of EG reduction at 20 min shows similar features to those of the $Cl_3^{2-}Pt-PtCl_3^{2-}$ dimer, particularly for the shape and the position of the peak at ∼11578 eV (marked by blue dash). Instead, the spectrum of CA reduction at 40 min is well described by a linear combination of the spectra of the initial K_2PtCl_4 and the naked Pt cluster with the fcc structure. Moreover, we have performed density functional theory (DFT) calculations for the optical absorption spectrum of the $Cl_3^{2-}Pt-PtCl_3^{2-}$ model (Figure 3d). It is clear that the calculated spectrum shows two prominent peaks at 224 and 249 nm. The 224 nm peak is similar to that at 220 nm in the experimental spectrum (Supporting Information Figure S2), which has been ascribed to Pt−Cl charge transfer. Importantly, the 249 nm peak in the calculation reproduces well the ∼250 nm peak in the experimental spectra for the EG reduction.

These results lead us to claim that the Pt−Pt pair formed in the initial nucleation stage of EG reduction is related to the $Cl_3^{2-}Pt-PtCl_3^{2-}$ dimer via metal−metal bonding between the partially reduced $PtCl_3^{2-}$ ions. With time increasing, these initially formed $Cl_3^{2-}Pt-PtCl_3^{2-}$ dimers would polymerize into a tetramer and the subsequent higher linear complexes "Pt_nCl_x" with more dimer units. We consider that the enhancement of the intermediate absorbance in UV−vis spectra can be ascribed to the increased number of aggregated dimers. Note that there is a remarkable red-shift of ca. 10 nm for the intermediate plasmon band. This is due to the aggregation of dimer clusters into larger linear "Pt_nCl_x" complexes with increasing dimensions, which lead to the enhancement of the longitudinal surface plasmon in the UV−vis spectra.[40,41] As the reactions proceed, after ∼100 min, the Pt−Pt coordination number increases quickly (e.g., at 200 min it is 5.0 as seen from Supporting Information Table S1), implying the formation of "Pt_nCl_x" complexes with a large number (n > 100) of Pt atoms.[42] In such a Pt cluster, the proportion of surface Cl^- atoms decreases sharply, and the effect of Cl^- capping on the surface is significantly lowered. Consequently, the intensity of absorbance at 255 nm originating from intermediate "Pt_nCl_x" complexes with high n gradually decreases from 120 min down to 240 min in the UV−vis spectra for the EG reduction.

Contrary to what was observed in the EG reduction, the nuclei formed in the CA reduction should come from the aggregation of Pt(0) atoms completely reduced from the precursor ions, a preferred evolution in the case of strong reductants.[43] These naked Pt_n^0 clusters exist separately in the reaction solution, weakly bonded with the surfactant PVP because no obvious contribution from a Pt−O bond can be found in the FT curves. Without other strong surfactant bonding, naked Pt_n^0 clusters show a significant contraction (2.6%) of the Pt−Pt bond length relative to that of Pt foil. In the later growth stage (>100 min), naked Pt_n^0 clusters grow in size. After ∼120 min, the Pt−Pt coordination number reaches 8.9 (Supporting Information Table S1), corresponding to a size of ∼3 nm. For these Pt_n^0 clusters the contraction of the Pt−Pt bond length is reduced due to the weakened nanosized effect compared with that of the initially formed small Pt_n^0 clusters (such as Pt_{20} or Pt_{30}, etc.). Therefore, at the later growth stage, the difference in Pt−Pt bond length between these two reactions reduces from 0.1 Å to 0.03 Å, as magnified in the insets of Figure 3a. Since the reduction of $PtCl_4^{2-}$ to Pt^0 is easier than that of $AuCl_4^-$ to Au^0 according to their standard electrical potentials of redox reactions (Supporting Information Table S2), the citric acid used here can be considered as a strong reductant relative to the case of the previous study.[26]

Summarizing the above results, two distinct nucleation pathways mediated by the reductants could be verified, as schematically shown in Figure 4. The scenario of the reductant-manipulated reduction reaction and of the nucleation process could be hypothesized as follows. When the weak reductant EG was used, the reduction rate would be substantially slowed

dx.doi.org/10.1021/ja302642x | J. Am. Chem. Soc. 2012, 134, 9410−9416

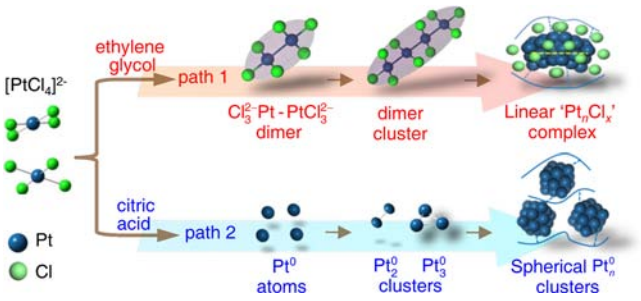

Figure 4. Schematic representations of reaction pathways manipulated by reductants. When the metal precursor $PtCl_4^{2-}$ ions are reduced by a weak reductant, ethylene glycol, the intermediate $Cl_3^{2-}Pt-PtCl_3^{2-}$ dimer and the subsequent dimer clusters and their aggregations into higher linear "Pt_nCl_x" complexes are formed in the nucleation stage, while for the relatively strong reductant citric acid, $PtCl_4^{2-}$ ions are reduced into Pt^0 atoms which then aggregated into Pt_2^0, Pt_3^0, and large Pt_n^0 clusters. The final shapes will be the nanowire and nanosphere, as expected, respectively.

down, and the $PtCl_4^{2-}$ ions may be partially reduced into $PtCl_3^{2-}$ ions first. Later two $PtCl_3^{2-}$ ions complex together via a metal–metal bond, forming a $Cl_3^{2-}Pt-PtCl_3^{2-}$ dimer cluster. Then, these preformed dimer clusters are polymerized to longer linear "Pt_nCl_x" complexes. Actually, this nucleation pathway is consistent with the previous prediction which suggested the formation of a $Pt^{II}-Pt^{I}$ dimer stabilized with Cl^- in the case of moderate reduction of K_2PtCl_4 precursor, based on the first-principles molecular dynamics simulations.[18] However, if a relatively stronger reductant CA was used, the $PtCl_4^{2-}$ ions can be reduced completely into zerovalent Pt^0 atoms which then aggregate into Pt_n^0 (such as Pt_{20}, Pt_{30}, etc.) clusters. As a result, the two distinct nucleation pathways significantly affect the NCs morphologies when the other reagents are the same. For the former case of the mild reaction, the linear cluster complex would easily lead to formation of a 1D nanostructure, such as nanowires, while, for the latter case of an intense reaction, the separated Pt_n^0 clusters are apt to produce a monodisperse nanospherical morphology. The conclusions drawn here greatly benefit from the complementary *in-situ* characterization methodologies—UV–vis spectroscopy, which gives us the direct evidence of the difference of the nucleation pathways induced by reductants, and XAFS, which further confirms and explains this phenomenon through our data analysis. Moreover, this combined method, in which the information is obtained at the same time on identical reaction solutions, guarantees the validity of the measurements.

We then turn to consider the dependence of the later growth and the shape of NCs on the aforementioned distinct nucleation pathways. It is noteworthy to mention that the Pt–Pt pair with a longer bond length in the $Cl_3^{2-}Pt-PtCl_3^{2-}$ dimer is analogous to the reported "aurophilic bond", which has a high directionality. In the synthesis of the 1D noble metal (such as Au and Pt) nanowires reported by Xia et al. and Yang et al., at the origin of the 1D oriented growth they proposed the formation of a linear chain complex composed of a M^I-M^I (M: Au or Pt) backbone with aurophilic interaction.[44,45] Accordingly, we consider that, in the slow EG reduction, more Pt dimer complexes could be attached to the initially formed $Cl_3^{2-}Pt-PtCl_3^{2-}$ dimer, forming a long-chain complex which would be converted into 1D Pt nanowires after further *in-situ* reduction. Moreover, the HRTEM image recorded on a single Pt nanowire (Figure 2a, inset) shows the lattice spacing between {111} planes of 0.23 nm, pointing out a growth of nanowires along the ⟨111⟩ direction, consistent with the previous reports.[44,45] Due to the formation of the long-chain complex "Pt_nCl_x", the nanowire displays a unique ⟨111⟩ growth direction, different from that of the conventional Au and Pd nanowires which typically grow along the ⟨100⟩ axis. On the contrary, during the strong CA reduction, the naked Pt_n^0 clusters are directly formed with no specific facets passivated or promoted, resulting in isotropic growth into a nearly spherical-like structure (Figure 2b). We consider that the formed chain polymer complexes and spherical free clusters served as the bases and are the prerequisites for the final shapes of NCs, respectively. But these alone are not enough. Although PVP has no contribution to the ~250 nm absorbance in the reduction, it plays an important role as the stabilizer. Particularly for the synthesis of Pt nanowires, besides the formed linear complexes mediated by the reductant EG in the initial nucleation stage, the stabilizer of PVP makes joint efforts to stabilize the formed dimer complex aggregated preferentially into the 1D chain in the later growth stage.[19,22] These results suggest that the initial nucleation heavily influences the growth process, thereby determining both the final shape and property of the resultant NCs.

■ CONCLUSION

Our *in-situ* probing has suggested that nucleation pathways can be tuned selectively by changing the strength of reductants, using a simultaneous measurement that combined quick-XAFS and UV–vis spectroscopies. To date, most of the available strategies are mainly focused on the manipulation of the later growth rather than initial nucleation, which involves two possible pathways. Our *in-situ* measurements show that the strength of reductant can be used to switch the nucleation between the two different pathways, which consequently has a great influence on the postgrowth dynamics and the final shapes of the obtained NCs. This ability to unveil the NCs formation mechanism would be helpful in guiding the controlled synthesis. For example, some supramolecular structures which are similar to our proposed "M_nR_x" (M, metal; R, anions) complexes can be preliminary synthesized as the precursors to prepare NCs with some specific shapes. Moreover, we have provided a feasible route on manipulating nucleation pathways which can also work to achieve the control for the morphologies and properties of nanostructures. It will be interesting to see if further studies can determine the 3D chemical structures of single clusters formed during the NCs formation, which may be answered by the development of an *in-situ* technique with combined high time and space resolutions.

■ ASSOCIATED CONTENT

Supporting Information

Schematic illustration of two nucleation pathways, UV–vis absorption spectra, k^2-weighted Pt L_3-edge EXAFS oscillations, XAFS fitting curves and parameters, the comparison of the positions of Pt–O and Pt–Cl FT peaks. This material is available free of charge via the Internet at http://pubs.acs.org.

■ AUTHOR INFORMATION

Corresponding Author

sqwei@ustc.edu.cn; yxie@ustc.edu.cn; wuzy@ustc.edu.cn

Author Contributions

[§]These authors contributed equally.

Notes

The authors declare no competing financial interest.

■ ACKNOWLEDGMENTS

This work was supported by the National Basic Research Program of China (No. 2009CB939901), the National Natural Science Foundation of China (11135008, 10725522, 11079004, 10605024, 11175184, 20701036, and 10734070), and the Knowledge Innovation Program of the Chinese Academy of Sciences (KJCX2-YW-N40 and KJCX2-YW-N42). The authors would like to thank NSRL and BSRF for the beam time.

■ REFERENCES

(1) Burda, C.; Chen, X.; Narayanan, R.; El-Sayed, M. A. *Chem. Rev.* **2005**, *105*, 1025−1102.
(2) Talapin, D. V.; Lee, J.-S.; Kovalenko, M. V.; Shevchenko, E. V. *Chem. Rev.* **2010**, *110*, 389−458.
(3) Tian, N.; Zhou, Z. Y.; Sun, S. G.; Ding, Y.; Wang, Z. L. *Science* **2007**, *316*, 732−735.
(4) Chen, A.; Holt-Hindle, P. *Chem. Rev.* **2010**, *110*, 3767−3804.
(5) Bratlie, K. M.; Lee, H.; Komvopoulos, K.; Yang, P.; Somorjai, G. A. *Nano Lett.* **2007**, *7*, 3097−3101.
(6) Lee, I.; Delbecq, F.; Morales, R.; Albiter, M. A.; Zaera, F. *Nat. Mater.* **2009**, *8*, 132−138.
(7) Sun, Y.; Xia, Y. *Science* **2002**, *298*, 2176−2179.
(8) Huang, X.; Li, S.; Huang, Y.; Wu, S.; Zhou, X.; Gan, C. L.; Boey, F.; Mirkin, C. A.; Zhang, H. *Nat. Commun.* **2011**, *2*, 292.
(9) Yin, Y.; Alivisatos, A. P. *Nature* **2005**, *437*, 664−670.
(10) Lim, B.; Jiang, M.; Tao, J.; Camargo, P. H. C.; Zhu, Y.; Xia, Y. *Adv. Funct. Mater.* **2009**, *19*, 189−200.
(11) Xia, Y.; Xiong, Y.; Lim, B.; Skrabalak, S. E. *Angew. Chem., Int. Ed.* **2009**, *48*, 60−103.
(12) Tao, A. R.; Habas, S.; Yang, P. *Small* **2008**, *4*, 310−325.
(13) Chen, J.; Herricks, T.; Xia, Y. *Angew. Chem., Int. Ed.* **2005**, *44*, 2589−2592.
(14) Sun, S. H.; Jaouen, F.; Dodelet, J. P. *Adv. Mater.* **2008**, *20*, 3900−3904.
(15) Finney, E. E.; Finke, R. G. *J. Colloid Interface Sci.* **2008**, *317*, 351−374.
(16) Kwon, S. G.; Hyeon, T. *Acc. Chem. Res.* **2008**, *41*, 1696−1709.
(17) LaMer, V. K.; Dinegar, R. H. *J. Am. Chem. Soc.* **1950**, *72*, 4847−4854.
(18) Colombi Ciacchi, L.; Pompe, W.; De Vita, A. *J. Am. Chem. Soc.* **2001**, *123*, 7371−7380.
(19) Li, F.; Gates, B. C. *J. Phys. Chem. B* **2004**, *108*, 11259−11264.
(20) Angermund, K.; Bühl, M.; Endruschat, U.; Mauschick, F. T.; Mörtel, R.; Mynott, R.; Tesche, B.; Waldöfner, N.; Bönnemann, H.; Köhl, G.; Modrow, H.; Hormes, J.; Dinjus, E.; Gassner, F.; Haubold, H.-G.; Vad, T.; Kaupp, M. *J. Phys. Chem. B* **2003**, *107*, 7507−7515.
(21) Watzky, M. A.; Finney, E. E.; Finke, R. G. *J. Am. Chem. Soc.* **2008**, *130*, 11959−11969.
(22) Mondloch, J. E.; Finke, R. G. *ACS Catal.* **2012**, *2*, 298−305.
(23) Sau, T. K.; Rogach, A. L. *Adv. Mater.* **2010**, *22*, 1781−1804.
(24) Pettibone, J. M.; Hudgens, J. W. *ACS Nano* **2011**, *5*, 2989−3002.
(25) Zheng, H.; Smith, R. K.; Jun, Y. W.; Kisielowski, C.; Dahmen, U.; Alivisatos, A. P. *Science* **2009**, *324*, 1309−1312.
(26) Yao, T.; Sun, Z.; Li, Y.; Pan, Z.; Wei, H.; Xie, Y.; Nomura, M.; Niwa, Y.; Yan, W.; Wu, Z.; Jiang, Y.; Liu, Q.; Wei, S. *J. Am. Chem. Soc.* **2010**, *132*, 7696−7701.
(27) Newton, M. A.; Belver-Coldeira, C.; Martinez-Arias, A.; Fernandez-Garcia, M. *Nat. Mater.* **2007**, *6*, 528−532.
(28) Harada, M.; Kamigaito, Y. *Langmuir* **2011**, *28*, 2415−2428.
(29) Harada, M.; Einaga, H. *Langmuir* **2006**, *22*, 2371−2377.
(30) Abécassis, B.; Testard, F.; Kong, Q.; Baudelet, F.; Spalla, O. *Langmuir* **2010**, *26*, 13847−13854.
(31) Hubert, F.; Testard, F.; Thill, A.; Kong, Q.; Tache, O.; Spalla, O. *Cryst. Growth Des.* **2012**, *12*, 1548−1555.
(32) Newville, M. *J. Synchrotron Radiat.* **2001**, *8*, 322.
(33) Ravel, B.; Newville, M. *J. Synchrotron Radiat.* **2005**, *12*, 537−541.
(34) Elding, L. I.; Olsson, L. F. *J. Phys. Chem.* **1978**, *82*, 69−74.
(35) Henglein, A.; Giersig, M. *J. Phys. Chem. B* **2000**, *104*, 6767−6772.
(36) Lee, I.; Morales, R.; Albiter, M. A.; Zaera, F. *Proc. Natl. Acad. Sci.* **2008**, *105*, 15241−15246.
(37) Knecht, M. R.; Weir, M. G.; Myers, V. S.; Pyrz, W. D.; Ye, H.; Petkov, V.; Buttrey, D. J.; Frenkel, A. I.; Crooks, R. M. *Chem. Mater.* **2008**, *20*, 5218−5228.
(38) Liu, X.; Bauer, M.; Bertagnolli, H.; Roduner, E.; van Slageren, J.; Phillipp, F. *Phys. Rev. Lett.* **2006**, *97*, 253401.
(39) Yamamoto, K.; Imaoka, T.; Chun, W.-J.; Enoki, O.; Katoh, H.; Takenaga, M.; Sonoi, A. *Nat. Chem.* **2009**, *1*, 397−402.
(40) El-Sayed, M. A. *Acc. Chem. Res.* **2001**, *34*, 257−264.
(41) Kim, F.; Song, J. H.; Yang, P. *J. Am. Chem. Soc.* **2002**, *124*, 14316−14317.
(42) Roldan Cuenya, B.; Croy, J. R.; Mostafa, S.; Behafarid, F.; Li, L.; Zhang, Z.; Yang, J. C.; Wang, Q.; Frenkel, A. I. *J. Am. Chem. Soc.* **2010**, *132*, 8747−8756.
(43) Duff, D. G.; Edwards, P. P.; Johnson, B. F. G. *J. Phys. Chem.* **1995**, *99*, 15934−15944.
(44) Chen, J.; Herricks, T.; Geissler, M.; Xia, Y. *J. Am. Chem. Soc.* **2004**, *126*, 10854−10855.
(45) Huo, Z.; Tsung, C. K.; Huang, W.; Zhang, X.; Yang, P. *Nano Lett.* **2008**, *8*, 2041−2044.